Nano Research

ISSN 1998-0124 CN 11-5974/O4
https://doi.org/10.1007/s12274-021-3945-3

Research Article

Exploring ternary organic photovoltaics for the reduced nonradiative recombination and improved efficiency over 17.23% with a simple large-bandgap small molecular third component

Huanran Feng[1] (✉), Yvjie Dai[1], Lihao Guo[1], Di Wang[2], Hao Dong[2], Zhihui Liu[1], Lu Zhang[1], Yvjin Zhu[1], Chen Su[1], Yongsheng Chen[3], and Weiwei Wu[1] (✉)

[1] *School of Advanced Materials and Nanotechnology, Interdisciplinary Research Center of Smart Sensors, Xidian University, Shaanxi 710126, China*
[2] *Intelligent Perception Research Institute, Zhejiang Lab, Hangzhou 311100, China*
[3] *State Key Laboratory and Institute of Elemento-Organic Chemistry, Key Laboratory of Functional Polymer Materials, College of Chemistry, Nankai University, Tianjin 300071, China*

Received: 27 September 2021 / **Revised:** 16 October 2021 / **Accepted:** 21 October 2021

ABSTRACT

Ternary strategy is one of the most effective methods to further boost the power conversion efficiency (PCE) of organic photovoltaic cells (OPVs). In terms of high-efficiency PM6:Y6 binary systems, there is still room to further reduce energy loss (E_{loss}) through regulating molecular packing and aggregation by introducing a third component in the construction of ternary OPVs. Here we introduce a simple molecule BR1 based on an acceptor-donor-acceptor (A-D-A) structure with a wide bandgap and high crystallinity into PM6:Y6-based OPVs. It is proved that BR1 can be selectively dispersed into the donor phase in the PM6:Y6 and reduce disorder in the ternary blends, thus resulting in lower $E_{loss,non\text{-}rad}$ and E_{loss}. Furthermore, the mechanism study reveals well-develop phase separation morphology and complemented absorption spectra in the ternary blends, leading to higher charge mobility, suppressed recombination, which concurrently contributes to the significantly improved PCE of 17.23% for the ternary system compared with the binary ones (16.21%). This work provides an effective approach to improve the performance of the PM6:Y6-based OPVs by adopting a ternary strategy with a simple molecule as the third component.

KEYWORDS

organic photovoltaic, ternary bulk heterojunction, nonradiative recombination, simple small molecule, phase separation

1 Introduction

Organic photovoltaic cells (OPVs) provide a promising route toward cost-effective, lightweight, and flexible photovoltaic cells which convert the energy of sunlight into electricity [1–4]. Recent years have witnessed remarkable progress in OPVs driven by the ongoing development of materials and device engineering, especially for the evolution of non-fullerene acceptors [5–10]. As one of the important milestones of the recent progress of OPVs, Y6-based devices become the focus of research [11–13]. The power conversion efficiency (PCE) of OPVs have been pushed over 18% with non-fullerene molecule Y6 and derivatives as acceptors [14–17].

To achieve further improvement in PCE, the concept of ternary OPVs —introduction of the third component in the donor/acceptor host —has increased momentum over the recent years. On the one hand, the third component could broaden the absorption, adjust the energy levels, modulate molecular stacking behavior, and donor/acceptor phase separation, contributing to the more electron-hole pair, better charge carrier separation, and transport, thus beneficial for obtaining the improved PCE [14, 18–22]. On the other hand, despite numerous studies, so far, the photovoltaic performance of OPVs is still lagging behind their inorganic semiconductors and perovskite counterparts, which can be partly attributed to the relatively large energy loss (E_{loss}) [23, 24]. It has been demonstrated that E_{loss} results mainly from energy losses during charge separation and non-radiative recombination ($E_{loss,rad}$ and $E_{loss,non\text{-}rad}$) [24]. In recent years, by reducing the energy offset between donor and acceptor molecular states and elevating the charge transfer state, $E_{loss,rad}$ can be minimalized and negligible [25–27]. How to reduce $E_{loss,non\text{-}rad}$ has been another important determining factor of the performance of OPVs. It is known that $E_{loss,non\text{-}rad}$ correlates directly with the external radiative efficiency of the electroluminescence (EQE_{EL}) of the solar cells [28, 29]. The ternary strategy with addition of the third component provides a new way to reduce the $E_{loss,non\text{-}rad}$ and E_{loss} beyond the design of novel and matched donor and acceptor materials. The third component could be conjugated polymers, small molecules, and quantum dots [30–33]. Among these, small molecules featuring fused-heterocyclic rings core and similar structures with acceptors in binary hosts are most commonly used third component due to their easier controllability and better compatibility with binary systems than those of polymers. For example, based on good compatibility with acceptor Y6, a series of Y6 derivatives and acceptor-donor-acceptor (A-D-A) structural acceptors were added into the PM6:Y6 blends as the third component for

Address correspondence to Huanran Feng, hrfeng@xidian.edu.cn; Weiwei Wu, wwwu@xidian.edu.cn

complementary absorption, better phase separation morphology, and more efficient exciton separation, thus boosting the PCE of ternary devices to over 17% [17, 34]. Meanwhile, optimized phase separation morphology and higher EQE_{EL} of these ternary devices reaching over 10^{-4} enable $E_{loss,non-rad}$ (< 0.3 eV) much lower than that (> 0.4 eV) of fullerene-based OPV cells [14].

In addition to small molecular non-fullerene acceptors featuring fused-heterocyclic rings core, much attention has also been recently attracted to small molecules based on simple structures with a wide bandgap and relative high crystallinity due to their easier synthesis with low cost and ability to efficiently optimize the morphology of active layers [35–38]. For instance, Hou et al. designed a wide-bandgap small molecule, NRM-1, with a series of binary blends for the study of reducing $E_{loss,non-rad}$. NRM-1 optimized the phase separation morphology and then resulted in enhanced EQE_{EL} of the ternary blends [31]. This, coupled by up-shift charge transfer state and complementary absorption, contributed to improving performance of ternary OPV devices with lower $E_{loss,rad}$ and $E_{loss,non-rad}$. Yang et al. fabricated ternary devices by introducing a series of molecules based on benzo[1,2-b:4,5-b']dithiophene core with structurally different π-conjugation systems [39]. This study demonstrated different working mechanisms of ternary devices based on these small molecules including alloy-like model, charge transfer, and energy transfer, respectively. As a result, the ternary OPV devices introducing SM-X with a horizontal-type push-pull structure as the third component achieved much higher PCE than binary devices. Inspired by this, Tang et al. introduced dithieno [3,2-b:2',3'-d]pyrrole-rhodanine molecule DR8 with high compatibility of PM6 into PM6:ITIC-4Cl [37]. Fine-tuning blend morphology with better phase separation and a well-formed fibrillar structure of the ternary blends yielded a PCE of 14.94% in comparison to host binary devices (13.52%). In addition, introducing DR8 into PM6:Y6 binary systems exhibited improved PCE of 16.73% with all simultaneously improved photovoltaic parameters. These studies of adding the third component based on a simple A-D-A structure with a wide bandgap and high crystallinity offer a new insight toward phase separation morphology modulation and E_{loss} reduction in non-fullerene OPVs and provide more opportunities to develop high-performance OPVs.

In this work, an A-D-A structure-based simple molecule BR1 using benzo[1,2-b:4,5-b']dithiophene as a central unit was chosen as the third component to be incorporated into the PM6:Y6 host blend. The introduction of BR1 into the PM6:Y6 blends simultaneously optimized the photo harvesting in the short-wavelength region and phase separation morphology. BR1 mixed preferentially with the PM6 matrix and possessed excellent ability to regulate molecular packing and aggregation in the ternary blends, leading to enhanced EQE_{EL}, reduced $E_{loss,non-rad}$, and improved photovoltaic performance. The OPVs based on ternary blends show a lower E_{loss} of 0.534 eV with the reduced $E_{loss,non-rad}$ of ca. 0.224 eV. Thanks to these advantages, the optimized PM6:Y6:BR1 based ternary OPVs demonstrated a high PCE of 17.23% with an open-circuit voltage (V_{oc}) of 0.859 V, a short-circuit current (J_{sc}) of 26.49 mA·cm^{-2}, and a fill factor (FF) of 75.7%, which is superior to those of the control binary devices (PCE of 16.21%, V_{oc} of 0.847 V, J_{sc} of 26.09 mA·cm^{-2}, and FF of 73.4%). The improvement in the J_{SC} and FF were attributed to the effective exciton dissociation and charge transport, lower bimolecular recombination, and optimized morphology. The result further confirms the great potential of ternary strategy by introducing the wide-bandgap small molecule with high crystallinity in achieving higher-performance OPVs.

2 Results and discussion

The chemical structures of PM6, Y6, and BR1 are present in Fig. 1(a), and the detailed synthetic route of BR1 is presented (Fig. S1 in the Electronic Supplementary Material (ESM)). BR1 has a high decomposition temperature over 390 °C determined by thermogravimetric analysis (Fig. S1 in the ESM), suggesting its good thermal stability for application in OPVs. The normalized ultraviolet-visible (UV–vis) absorption spectra of PM6, Y6, and BR1 in the film state are shown in Fig. 1(b). PM6 displays a strong absorption in the range of 500–650 nm and a broad light absorption ranging from 600–950 nm is shown by Y6. BR1 has a complementary absorption band in the short-wavelength region from 400 to 550 nm, which can be beneficial for light absorption in the short band and therefore higher photoproduced current in the ternary devices. BR1 possesses a planar structure with four alkyl side chains stretching in lateral conformation revealed by the density functional theory (DFT) calculation at B3LYP/6-31G(d,p) level. Both the highest occupied molecular orbital (HOMO) and

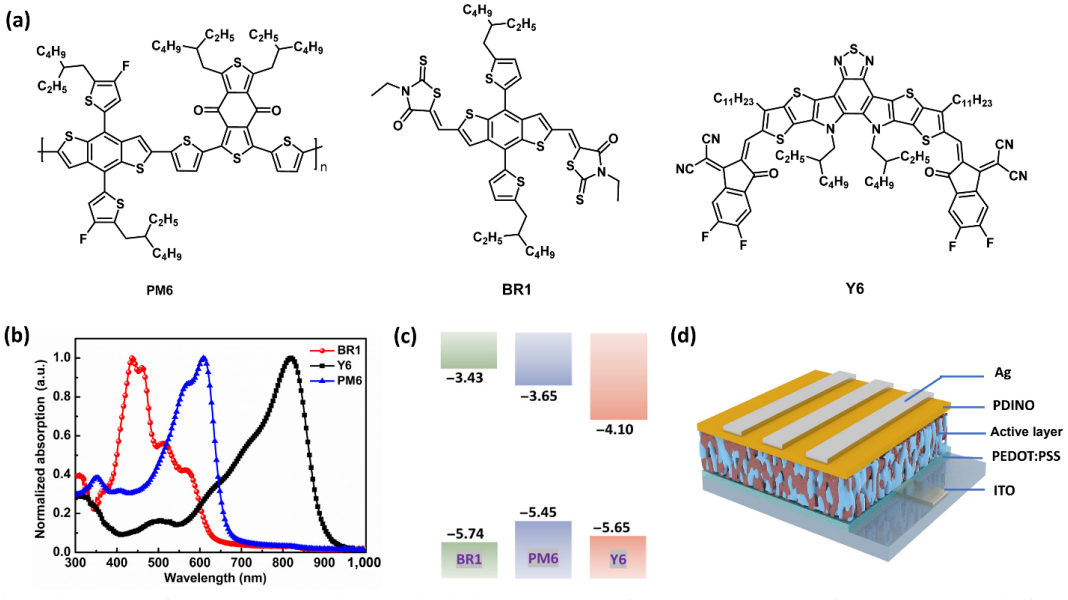

Figure 1 (a) Chemical structures of PM6, BR1, and Y6. (b) Normalized absorption spectra of neat PM6, BR1, and Y6 films. (c) Energy levels of PM6, BR1, and Y6. (d) Schematic structure diagram of OPVs.

lowest unoccupied molecular orbital (LUMO) distribute along the backbone chain as can be seen from Fig. S4 in the ESM. The exposed conjugated skeleton enables the ability to regulate molecular packing and aggregation for BR1. The electronic energy levels of BR1, PM6, and Y6 are depicted in Fig. 1(c).

The photovoltaic properties of binary and ternary organic solar cells based on PM6:Y6 and PM6:Y6:BR1 were investigated with the device structure ITO/PEDOT:PSS/active layer/PDINO/Ag. The current density–voltage (*J*–*V*) curves of the optimized devices measured under AM1.5G irradiation at an intensity of 100 mW·cm^{-2} are shown in Fig. 2(a) and the detailed photovoltaic performance parameters of the corresponding devices are given in Table 1 and Table S1 in the ESM. The optimal binary solar cells of PM6:Y6 (1:1.2, w/w) exhibits V_{oc} of 0.847 V, J_{sc} of 26.09 mA·cm^{-2} and FF of 73.4%, which is comparable to the values reported [11]. Upon the addition of 10 wt.% of BR1 (based on the weight of PM6 in binary blends) into the PM6:Y6 blends, the ternary devices shows an obvious enhancement in all photovoltaic performance parameters, with V_{oc} of 0.859 V, J_{sc} of 26.49 mA·cm^{-2} and FF of 75.7%, resulting in a significantly improved PCE of 17.23%. As shown in Table S1 in the ESM, the V_{oc} of ternary devices gradually improve with the increasing BR1 content in the ternary blends which benefited from the relatively higher-lying HUMO level of BR1 [36]. The average PCE of the optimized binary and ternary devices are 15.95% and 17.02% according to 30 individual OPV devices (Fig. 2(b)), respectively, confirming the positive roles of BR1 on performance improvement of the OPV devices. The performance boost can be mainly attributed to the enhanced photon harvesting, exciton dissociation, and charge transport, as well as the reduced E_{loss} in the ternary OPV compared to the PM6-based binary devices, as discussed below. Figure 2(c) shows the corresponding external quantum efficiency (EQE) spectra of the best binary and ternary cells. The ternary devices exhibits higher EQE in the short wavelength range of 400–550 nm than that of binary cells which results in improved J_{sc} and can be attributed to the enhanced optical absorption of BR1. The J_{sc} integrated from the EQE spectra curves are 25.21 and 25.48 mA·cm^{-2} for the binary and ternary cells, respectively, which are similar to the measured J_{sc} values in the permitted range of error suggesting the good reliability of the *J*–*V* measurements.

The effect of the introduction of BR1 on the energy loss of the cells was investigated and the detailed parameters have been summarized in Table 2. The E_g of the OPV devices was estimated according to the intersections between the absorption and emission of the acceptors (Fig. S6 in the ESM) [40, 41]. The optimized ternary devices with BR1 incorporation shows a decreased E_{loss} of 0.534 eV compared with that of binary ones (0.552 eV) based on the binary ones. Generally, an E_{loss} can be split up into three terms (ΔE_1, ΔE_2, and ΔE_3) and the third part of energy loss ΔE_3 (i.e., $E_{loss,non\text{-}rad}$) induced by nonradiative recombination can be estimated via EL emission characterization [24, 42]. As shown in Fig. 2(f), the EQE_{EL} values of ternary improves from 0.014% to 0.017% after adding BR1, thus the corresponding ΔE_3 can be calculated to be 0.229 and 0.224 eV for binary and ternary OPVs, respectively. Couple with ΔE_1 are calculated to be 0.268 and 0.262 eV according to

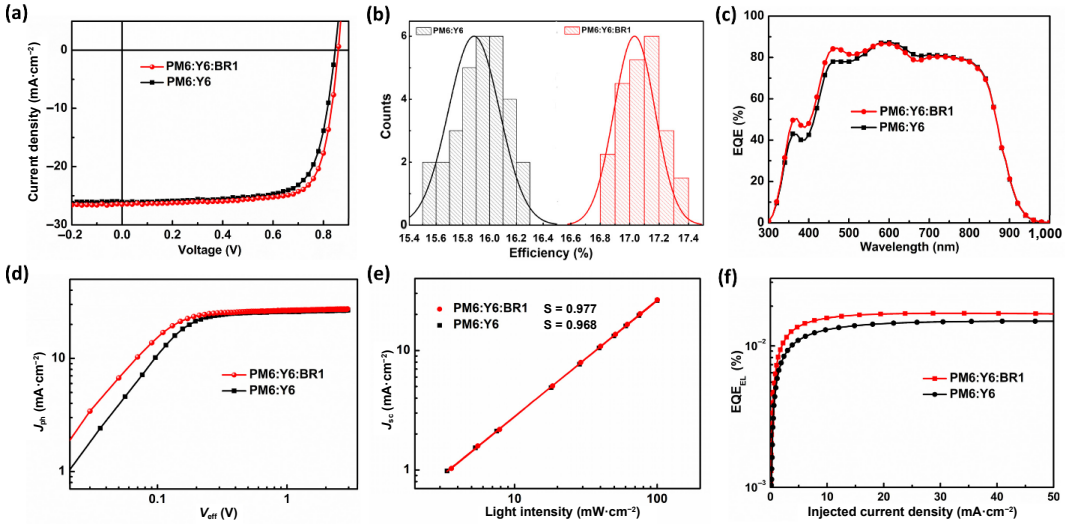

Figure 2 (a) Current density–voltage (*J*–*V*) curves for the devices based on PM6:Y6 and PM6:Y6:BR1 at optimized conditions under the illumination of AM 1.5G (100 mW·cm^{-2}), (b) the histograms of the PCE counts for 30 devices, (c) EQE curves for the PM6:Y6 and PM6:Y6:BR1 based OPV devices, (d) J_{ph} versus V_{eff}, (e) light intensity (P) dependence of J_{sc} for the optimized devices, and (f) external quantum efficiency of EL (EQE_{EL}) of the PM6:Y6 and PM6:Y6:BR1 devices.

Table 1 Optimal device parameters of PM6:Y6 and PM6:Y6:BR1 based devices under the illumination of AM 1.5G (100 mW·cm^{-2})

BHJ layer	V_{oc} (V)[a]	J_{sc} (mA·cm^{-2})[a]	FF (%)[a]	PCE (%)[a]	μ_e (cm^2·V^{-1}·s^{-1})	μ_h (cm^2·V^{-1}·s^{-1})	μ_e/μ_h
PM6:Y6	0.847 (0.846 ± 0.05)	26.09 (25.80 ± 0.30)	73.4 (72.7 ± 0.85)	16.21 (15.95 ± 0.30)	4.83	2.30	2.10
PM6:Y6:BR1	0.859 (0.856 ± 0.04)	26.49 (26.30 ± 0.25)	75.7 (75.1 ± 0.80)	17.23 (17.02 ± 0.20)	5.97	3.26	1.83

[a] Average values with standard deviations obtained from 30 devices are provided in the parentheses.

Table 2 Summary of the energy-loss parameters for the binary PM6:Y6 and ternary PM6:Y6:BR1 OPVs

BHJ layer	E_g/q (eV)	E_{loss} (eV)	ΔE_1 (eV)	EQE_{EL}·exp	ΔE_3 (eV)	ΔE_2 (eV)[a]
PM6:Y6	1.399	0.552	0.268	0.014%	0.229	0.055
PM6:Y6:BR1	1.393	0.534	0.262	0.017%	0.224	0.048

[a] ΔE_2 roughly estimated from $E_{loss}-\Delta E_1-\Delta E_3$.

Shockley–Queisser limit [43], these data suggest ΔE_2 of ternary devices is also reduced from 0.055 to 0.048 eV. Thus the BR1 introduction can effectively reduce the E_{loss} of devices based on PM6:Y6 systems.

To further investigate the effect of BR1 incorporation on charge generation and transport in active layers, the photocurrent (J_{ph}) versus the effective applied voltage (V_{eff}) for the binary and ternary devices was measured as shown in Fig. 2(d). It was generally considered that the efficiency of photogenerated excitons dissociation and charge carrier collection by electrodes was 100% at high bias V_{eff} ($V_{eff} \geq 2$ V) and J_{sat} should be primarily determined by the total photogenerated exciton density [44]. The ternary devices exhibit a higher saturated current density (J_{sat}) than binary ones (27.20 vs. 26.70 mA·cm^{-2}), which can be attributed to slightly enhanced photon harvesting in the former. The exciton dissociation and charge collection probability can be estimated from the ratio of J_{ph}/J_{sat} under the short circuit conditions and at the maximal output point. The PM6:Y6 based binary and ternary cells exhibit J_{ph}/J_{sat} of 0.972 and 0.974 under short circuit conditions, respectively. In addition, the J_{ph}/J_{sat} ratio at the maximal output point for binary and ternary cells is calculated to be 0.862 and 0.885, respectively. This result indicates that the introduction of BR1 as the third component improves the exciton dissociation and charge collection efficiency. Transient photocurrent (TPC) decay kinetics is studied to further probe the effect of BR1 incorporation on charge extraction process. As shown in Fig. 3(a), the devices with 10% BR1 addition shows 0.52 μs for charge extraction time, which is less than that of control binary ones (0.74 μs). Thus BR1 addition promoted the charge extraction, which is favorable to the enhancement of FF and J_{sc}.

The light intensity dependence of J_{sc} was also exploited to investigate influence of introducing BR1 on the charge recombination mechanisms as shown in Fig. 2(e). The value of photocurrent J_{sc} followed a power law dependence with respect to light intensity P_{light} which can be expressed as $J_{sc} \propto P_{light}^{S}$, and the bimolecular recombination appears to be lower when S value is close to 1. The exponential factor S of 0.977 for the ternary cells with BR1 addition is higher than that of 0.968 for binary cells, suggesting weak bimolecular recombination in ternary cells with BR1 introduction, which is also consistent with its improved FF. As shown in Fig. S7 in the ESM, photoluminescence (PL) spectra of PM6 and BR1, and their blend films were measured with excitation at 470 nm. Obviously, the neat BR1 film exhibits a strong emission peak at 690 nm and PM6 exhibits a weak peak at 665 nm. The PL quenching of PM6:BR1 was clearly observed, indicating charge transfer occured at PM6/BR1 interfaces which was supported by little overlapped between the excitation spectrum of PM6 and emission spectrum of BR1. In addition, charge recombination dynamics of the devices were investigated using transient photovoltage (TPV) measurements as shown in Fig. 3(b). Ternary devices exhibit longer charge carrier lifetime (102.14 μs) compared with that (82.58 μs) of control binary devices, which further indicate the positive effects of BR1 in reducing the bimolecular recombination loss. The hole mobility (μ_h) and electron mobility (μ_e) in optimal binary and ternary blends films were measured by space charge limited current (SCLC) method (Fig. S5 in the ESM). The control binary blend exhibits a μ_h of 2.30 × 10^{-4} cm^2·V^{-1}·s^{-1} and a μ_e of 4.83 × 10^{-4} cm^2·V^{-1}·s^{-1} with a μ_e/μ_h of 2.1. After adding BR1 into the binary systems, both parameters show a tendency to increase with the values of 3.26 × 10^{-4} cm^2·V^{-1}·s^{-1} and 5.97 × 10^{-4} cm^2·V^{-1}·s^{-1}, respectively, along with a more balanced μ_e/μ_h of 1.83. The enhancement on charge carrier with BR1 incorporating can be attributed to the improved film morphology with more efficient electron and hole transport channels in the subsequent discussion.

To understand the working mechanism of BR1 as the third component in tuning the morphology of PM6:Y6 blends, the miscibility between BR1 and PM6 and Y6 was investigated by evaluating the surface energy (γ) via contact angles measurement of water and glycerol on each neat film as shown in Fig. 4 with the parameters of surface energy displayed in Table S2 in the ESM [45–47]. According to the model of Wu, the γ was calculated to be 21.8, 20.4, and 27.7 mN·m^{-1} for PM6, BR1, and Y6, respectively. Then the miscibility of blends can be estimated by the Flory–Huggins interaction parameter χ, which is calculated by the equation $\chi_{1,2} \propto (\sqrt{\gamma_1} - \sqrt{\gamma_2})^2$ [48]. The χ parameter of the PM6:BR1 blend film is 0.024, which is much lower than 0.57 of Y6:BR1 blend and 0.36 of the PM6:Y6 blends, suggesting that BR1 has higher miscibility with PM6 compared to Y6. The accurate location of BR1 in the blend film was further predicted by calculation of the wetting coefficient (ω) from the interfacial surface energy based on Young's equation and Neumann's equation [47, 49, 50]. The ω value of BR1 in the blend of PM6 and Y6 was calculated to be 1.49, which indicates that the BR1 trends to be embedded together with PM6 to optimize phase separation morphology in the ternary blends. The absorption spectra of the blend film of PM6:BR1 and Y6:BR1 with different weight ratios were measured. As shown in Fig. 4(b), for the pristine PM6 film, the main absorption peak is at 609 nm with a shoulder peak at ~ 560 nm. By increasing the feed ratio of BR1 in the PM6:BR1 blend films from 1:0 to 1:1, the absorption signal of BR1 appeared in the short-wavelength region and the shoulder peak of PM6 increased gradually along with signal peak redshift from 609 to 628 nm. However, the absorption peak of Y6 was not affected by the varying feed ratio of BR1. This result implies that BR1 can mix with PM6 at the molecular level while relative larger phase separation may occur in the Y6:BR1 blends. Meanwhile, it can be speculated that reorganization at the bulk heterojunction interfaces in the ternary blends has occurred: The BR1 pushes the Y6 away from the mixed amorphous phase, and thus results pure acceptor domains as well as reduced disorder in the ternary blends [51]. In addition, the χ between PM6 and Y6:BR1 mixtures was calculated to be 0.530, which is higher than that of PM6:Y6. Likewise, a higher χ of 0.403 between PM6:BR1 mixtures and Y6

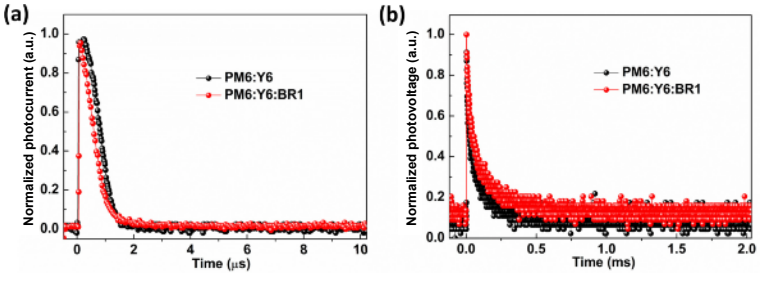

Figure 3 (a) Transient photocurrent and (b) transient photovoltage measurements of PM6:Y6 and PM6:Y6:BR1 based devices.

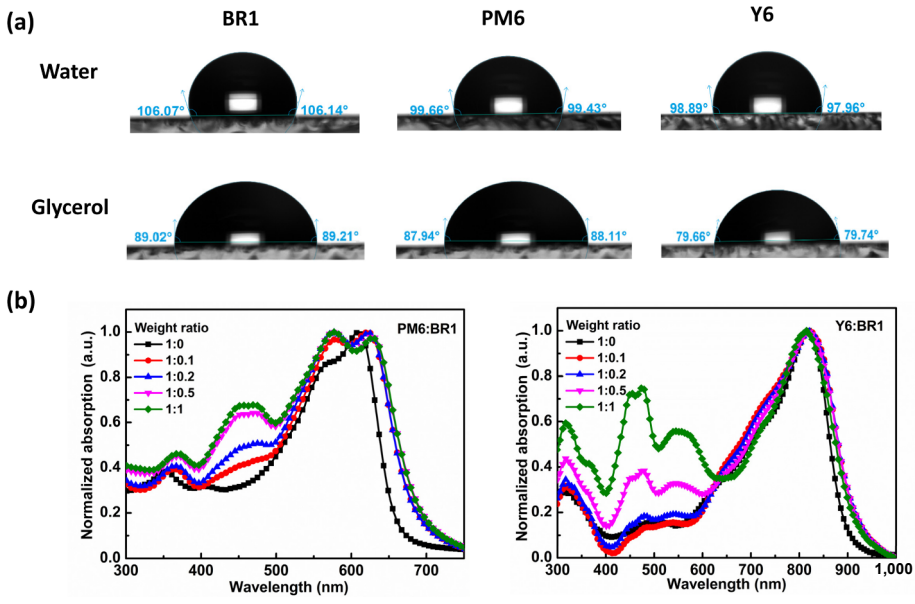

Figure 4 (a) The images of water and glycerol drops on PM6, BR1, and Y6 films. (b) Normalized absorption spectra of the PM6:BR1 and Y6:BR1 blend films.

was obtained and higher than that of Y6:BR1 (Fig. S8 in the ESM). This result implies that the addition of BR1 reduce the miscibility between PM6 and Y6, which results in large phase separation in the PM6:Y6:BR1 blend film as discussed in following morphology measurement due to the high crystallinity of BR1 [52, 53].

The surface and bulk morphology of the binary and ternary blend films are characterized by using atomic force microscopy (AFM) and transmission electron microscopy (TEM), respectively. As shown in Fig. 5(a), the control binary and ternary blends both display a smooth surface with similar root mean square roughness of 1.05 and 1.11 nm, respectively. Similar root-mean-square (RMS) roughness value confirms the homogeneous morphology of ternary blend film based on PM6:Y6:BR1. It suggests that BR1 is finely mixed with the host blend which is consistent with the former miscibility measurement. TEM measurement results reveal that ternary blends with BR1 as morphology regulator displays favorable fiber-like structures with appropriate aggregates and better developed phase separation compared with control binary blends. The well-developed microstructure morphology of ternary blends can provide more donor/acceptor interfaces and construct

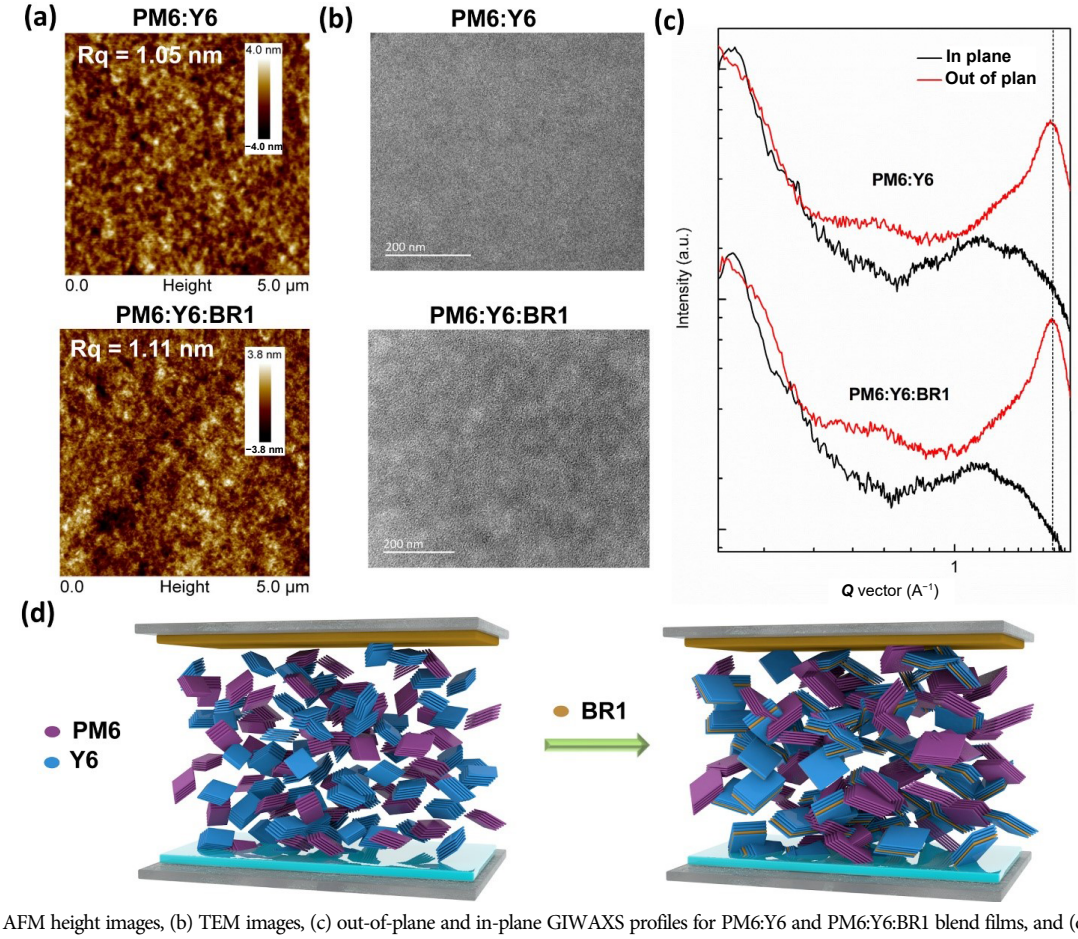

Figure 5 (a) AFM height images, (b) TEM images, (c) out-of-plane and in-plane GIWAXS profiles for PM6:Y6 and PM6:Y6:BR1 blend films, and (d) the schematic of morphology evolution from PM6:Y6 to PM6:Y6:BR1.

more efficient charge transport channels, which is desirable for exciton separation and charge transport thus facilitating the improvement of J_{sc} and FF.

Grazing-incidence wide-angle X-ray scattering (GIWAXS) is performed to further investigate the influence of BR1 addition on molecular packing in active films. As shown in Fig. 5(c), the diffraction peaks of PM6 largely overlap with those of Y6 in both binary and ternary films, and therefore only analysis of peak summation can be performed. As shown in Fig. S9 in the ESM, the neat BR1 film exhibits a series of strong anisotropic multiple diffractions, indicating its polycrystalline structure. The PM6:Y6 blend film shows a lamellae ordering (100) peak at 0.28 $Å^{-1}$ in the in-plane (IP) direction and π–π stacking ordering (010) peak at 1.74 $Å^{-1}$ in out-of-plane (OOP) direction, indicating a preferential face-on orientation was adopt for the PM6:Y6 blend film. This favorable face-on orientation is beneficial for charge transport in active layers thus maintaining device performance in the ternary system. After incorporating BR1, the ternary blend film exhibits a slightly stronger diffraction peak of lamellar stacking at 0.28 $Å^{-1}$ with a higher crystal coherence length (CCL) of 18.8 Å than that of control film (11.3 Å). The π–π stacking peak moves to 1.76 Å, corresponding with a decreased π–π stacking distance of 3.57 Å compared to 3.61 Å of control blends. The CCL of (010) peak of PM6:Y6 and PM6:Y6:BR1 systems are calculated to be 17.7 and 19.5 Å, respectively. The enhanced CCL in the ternary system corresponds to an increased crystallinity and suggests a better phase separation, which is responsible for the increased charge mobility. These results indicate that the introduction of BR1 can enable more compacted π–π stacking and higher crystallinity of the active layers, which is advantageous for improving exciton separation and charge transport, eventually improving the photovoltaic performance. The GIWAXS, AFM, and TEM results together demonstrate the favorable effects of BR1 addition on host binary blend film. The schematic of morphology evolution can be explained as in Scheme 2, the BR1 endows the ternary system with stronger crystallinity and more obvious and uniformed phase separation and leads to the improvement of charge separation and transport in the corresponding OPV device.

3 Conclusions

In summary, we successfully applied a simple A-D-A structure molecule BR1 with a wide bandgap and high crystallinity as third component into PM6:Y6 based binary OSC devices to regulate molecular packing and aggregation in the blend for lower E_{loss} and higher performance. BR1 possesses strong absorption in the near ultraviolet region and good compatibility of PM6 and trends to increase the phase separation, produce enhanced photon harvesting in short-wavelength region and modified morphology with a well-formed fibrillar structure. Through systematic investigation of the molecular packing and aggregation, charge transport and recombination properties of the ternary devices, it is believed that the addition of BR1 reduces the π–π stacking distance, promotes exciton dissociation, improves charge transport, inhibits charge recombination as well as enhance electroluminescence emission, thereby the optimized ternary OPVs exhibit a high PCE of 17.23% with E_{loss} of 0.534 eV, significantly higher than those values of binary ones. The results indicate that BR1 is a promising third component in further improving the performance of the PM6:Y6 based OPVs. With the simple fabrication process of ternary OPVs, simple synthesis and multiple beneficial functions of the BR1, this strategy can be easily applied for the large-scale production of OPVs.

4 Experimental section

4.1 Materials and synthesis

All reactions and manipulations were carried out under argon atmosphere with the use of standard Schlenk techniques. The solvents were purified and dried according to standard procedures. Donor polymer PM6 and Y6 were purchased from Solarmer Materials Inc. The starting material—4,8-bis(5-(2-ethylhexyl)thiophen-2-yl)benzo[1,2-b:4,5-b']dithiophene-2,6-dicarbaldehyde was prepared according to Ref. [54]. The other materials were common commercial levels and used as received.

BR1 BDTT-CHO (200 mg), 3-Ethylrhodanine, and piperidine (0.3 mL) were dissolved in chloroform (45 mL). The reaction was stirred at 65 °C for several hour with process monitored by TLC. After reaction, the mixture was concentrated. The residue was purified by silica gel column chromatography (petroleum ether/dichloromethane = 1:1 v/v) to obtain a red solid (52%). ^{1}H nuclear magnetic resonance (NMR) (400 MHz, $CDCl_3$):δ 7.95 (s, 2H), 7.91 (s, 2H), 7.33 (d, 2H), 6.97 (d, 2H), 4.18–4.19 (m, 4H), 2.94–2.92 (d, 4H), 1.42 (m, 2H), 1.33–1.25 (m, 18H), and 1.00–0.93 (m, 16H). ^{13}C NMR (100 MHz, $CDCl_3$) δ 192.12, 167.12, 147.31, 141.82, 139.65, 137.41, 135.40, 131.30, 128.48, 125.98, 125.65, 125.44, 124.79, 41.50, 40.03, 34.32, 32.53, 28.93, 25.77, 23.07, 14.22, 12.29, and 10.97. MALDI-TOF: calcd for $C_{46}H_{52}N_2O_2S_8$ [M+], 921.4140; found: 921.1840.

4.2 Measurements and instruments

The ^{1}H and ^{13}C NMR spectra were taken on a Bruker AV400 spectrometer. Matrix assisted laser desorption/ionization time-of-flight (MALDI-TOF) mass spectrometry was performed on a Bruker Autoflex III instrument. Electrospray ionization mass spectrometry (ESI-MS) were performed on the Thermo Finnigan LCQ™ Advantage instrument. The thermogravimetric analysis (TGA) was carried out on a NETZSCH STA 409PC instrument under purified nitrogen gas flow. The heating rate for TGA testing is 10 °C·min^{-1}. Ultraviolet-visible (UV–vis) spectra was obtained with a JASCO V-570 spectrophotometer. Cyclic voltammetry (CV) experiments were performed with a CHI660E microcomputer-based electrochemical analyzer in dichloromethane solutions. All measurements were carried out at room temperature with a conventional three-electrode configuration employing a glassy carbon electrode as the working electrode, a saturated calomel electrode (SCE) as the reference electrode, and a Pt wire as the counter electrode. Tetrabutylammonium phosphorus hexafluoride (n-Bu_4NPF_6, 0.1 M) in dichloromethane was used as the supporting electrolyte, and the scan rate was 100 mV·s^{-1}. The HOMO and LUMO energy levels were calculated from the onset oxidation potential and the onset reduction potential, using the equation $E_{HOMO} = -(4.80 + E_{ox}^{onset})$, $E_{LUMO} = -(4.80 + E_{re}^{onset})$.

The geometry structures of BR1 were optimized by using DFT calculations (B3LYP/6-31G(d, p)), and the frequency analysis was followed to assure that the optimized structures were stable states. All calculations were carried out using Gaussian 09. AFM investigation was performed using Bruker MultiMode 8 in tapping mode. The TEM investigation was performed on JEM-2100F at 200 kV. The specimen for TEM measurement was prepared by spin casting the blend solution on ITO/PEDOT:PSS substrate, then floating the film on a water surface and transferring to TEM grids. GIWAXS measurement was performed at MetalJet-D2, excillum on the wavelength of 0.134144 nm with xeuss 2.0. All samples were deposited on the silicon and irradiated at a fixed X-ray incident angle of 0.2° with an exposure time of 1,800 s. Contact angles were measured on the neat donor and acceptor films with the contact angle meter (Theta Flex, Biolin) by using two different solvents (water and glycerol).

The hole and electron mobility were measured using the SCLC method, employing a diode configuration of ITO/PEDOT:PSS/active layer/Au for hole and glass/Al/active layer/Al for electron by taking the dark current density in the range of 0–8 V and fitting the results to a space charge limited form, where SCLC was described by:

$$J = \frac{9\varepsilon_0\varepsilon_r\mu_0 V^2}{8L^3} \quad (1)$$

where J is the current density, L is the film thickness of the active layer, μ is the hole or electron mobility, ε_r is the relative dielectric constant of the transport medium, ε_0 is the permittivity of free space (8.85×10^{-12} F·m^{-1}), V (= $V_{appl} - V_{bi}$) is the internal voltage in the device, where V_{appl} is the applied voltage to the device and V_{bi} is the built-in voltage due to the relative work function difference of the two electrodes.

The current density–voltage (J–V) characteristics of photovoltaic devices were obtained using a Keithley 2400 source-measure unit. The photocurrent was measured under illumination simulated 100 mW·cm^{-2} AM1.5G irradiation using a xenon-lamp-based solar simulator [Oriel 96000 (AM1.5G)] in an argon filled glove box. Simulator irradiance was characterized using a calibrated spectrometer and illumination intensity was set using a certified silicon diode. EQE values of the devices were measured using Stanford Research Systems SR810 lock-in amplifier.

4.3 Fabrication of OPV devices

The photovoltaic devices were fabricated with a structure of glass/ITO/PEDOT:PSS/Donor:Acceptor/PDINO/Ag. The ITO coated glass substrates were cleaned by detergent, deionized water, acetone, and isopropyl alcohol under ultrasonication for 15 min each and dried by a nitrogen blow. The PEDOT:PSS layer was spin-coated (ca. 30 nm thick) onto the cleaned ITO surface. The substrates were then placed into an argon-filled glove box after being baked at 150 °C for 20 min. PM6, Y6, and BR1 were dissolved in chloroform with different weight ratios. The total weight ratio of PM6:Y6 was kept at 1:1.2. 0.5 vol.% CN was used as the solvent additive for all solutions. The active layers were generated by spincoating the active layer solutions on the top of PEDOT:PSS layer with a thickness of 150 nm. The active layer thickness was measured using a Dektak150 profilometer. Subsequently, the active layers were heated at 100 °C for 10 min. And then, PDINO, with the concentration of 2.0 mg/mL using CH_3OH solvent, was spin-coated at 3,000 rpm for 40 s on the active layer. Finally, a 60 nm Ag layer was deposited on the PDINO layer under high vacuum (< 1.5×10^{-4} Pa). The effective area of each cell was 4 mm^2 as defined by shadow masks for the solar cell devices discussed in this work.

Acknowledgements

This work was financially supported by the National Natural Science Foundation of China (Nos. 22005234 and 61904134) and Zhejiang Lab (No. 2021MC0AB02).

Electronic Supplementary Material: Supplementary material (characterization data for the new compounds, thermogravimetric analysis, cyclic voltammogram, PL spectra, mobility test, GIWAXS measurement, contact angle characterizations details and data, NMR spectra, mass spectra, and other device data) is available in the online version of this article at https://doi.org/10.1007/s12274-021-3945-3.

References

[1] Meng, L. X.; Zhang, Y. M.; Wan, X. J.; Li, C. X.; Zhang, X.; Wang, Y. B.; Ke, X.; Xiao, Z.; Ding, L. M.; Xia, R. X. et al. Organic and solution-processed tandem solar cells with 17.3% efficiency. *Science* **2018**, *361*, 1094–1098.

[2] Yu, G.; Gao, J.; Hummelen, J. C.; Wudl, F.; Heeger, A. J. Polymer photovoltaic cells: Enhanced efficiencies via a network of internal donor-acceptor heterojunctions. *Science* **1995**, *270*, 1789–1791.

[3] Kan, B.; Ershad, F.; Rao, Z. Y.; Yu, C. J. Flexible organic solar cells for biomedical devices. *Nano Res.* **2021**, *14*, 2891–2903.

[4] Cheng, P.; Li, G.; Zhan, X. W.; Yang, Y. Next-generation organic photovoltaics based on non-fullerene acceptors. *Nat. Photonics* **2018**, *12*, 131–142.

[5] Zhang, Q.; Wan, X. J.; Xing, F.; Huang, L.; Long, G. K.; Yi, N. B.; Ni, W.; Liu, Z. B.; Tian, J. G.; Chen, Y. S. Solution-processable graphene mesh transparent electrodes for organic solar cells. *Nano Res.* **2013**, *6*, 478–484.

[6] Wang, J. Y.; Zhan, X. W. Fused-ring electron acceptors for photovoltaics and beyond. *Acc. Chem. Res.* **2021**, *54*, 132–143.

[7] Wadsworth, A.; Moser, M.; Marks, A.; Little, M. S.; Gasparini, N.; Brabec, C. J.; Baran, D.; McCulloch, I. Critical review of the molecular design progress in non-fullerene electron acceptors towards commercially viable organic solar cells. *Chem. Soc. Rev.* **2019**, *48*, 1596–1625.

[8] Yang, Y.; Feng, E. M.; Li, H. Y.; Shen, Z. C.; Liu, W. R.; Guo, J. B.; Luo, Q.; Zhang, J. D.; Lu, G. H.; Ma, C. Q. et al. Layer-by-layer slot-die coated high-efficiency organic solar cells processed using twin boiling point solvents under ambient condition. *Nano Res.* **2021**, *14*, 4236–4242.

[9] Mishra, A. Material perceptions and advances in molecular heteroacenes for organic solar cells. *Energy Environ. Sci.* **2020**, *13*, 4738–4793.

[10] Zhang, D. Y.; Fan, P.; Shi, J. Y.; Zheng, Y. F.; Zhong, J.; Yu, J. S. Control of vertical phase separation in high performance non-fullerene organic solar cell by introducing oscillating stratification preprocessing. *Nano Res.* **2021**, *14*, 1319–1325.

[11] Guo, Q.; Guo, Q.; Geng, Y. F.; Tang, A. L.; Zhang, M. J.; Du, M. Z.; Sun, X. N.; Zhou, E. J. Recent advances in PM6: Y6-based organic solar cells. *Mater. Chem. Front.* **2021**, *5*, 3257–3280.

[12] Yuan, J.; Zhang, Y. Q.; Zhou, L. Y.; Zhang, G. C.; Yip, H. L.; Lau, T. K.; Lu, X. H.; Zhu, C.; Peng, H. J.; Johnson, P. A. et al. Single-junction organic solar cell with over 15% efficiency using fused-ring acceptor with electron-deficient core. *Joule* **2019**, *3*, 1140–1151.

[13] Li, S. X.; Li, C. Z.; Shi, M. M.; Chen, H. Z. New phase for organic solar cell research: Emergence of Y-series electron acceptors and their perspectives. *ACS Energy Lett.* **2020**, *5*, 1554–1567.

[14] Bi, P. Q.; Zhang, S. Q.; Chen, Z. C.; Xu, Y.; Cui, Y.; Zhang, T.; Ren, J. Z.; Qin, J. Z.; Hong, L.; Hao, X. T. et al. Reduced non-radiative charge recombination enables organic photovoltaic cell approaching 19% efficiency. *Joule* **2021**, *5*, 2408–2419.

[15] Li, C.; Zhou, J. D.; Song, J. L.; Xu, J. Q.; Zhang, H. T.; Zhang, X. N.; Guo, J.; Zhu, L.; Wei, D. H.; Han, G. C. et al. Non-fullerene acceptors with branched side chains and improved molecular packing to exceed 18% efficiency in organic solar cells. *Nat. Energy* **2021**, *6*, 605–613.

[16] Liu, Q. S.; Jiang, Y. F.; Jin, K.; Qin, J. Q.; Xu, J. G.; Li, W. T.; Xiong, J.; Liu, J. F.; Xiao, Z.; Sun, K. et al. 18% Efficiency organic solar cells. *Sci. Bull.* **2020**, *65*, 272–275.

[17] Liu, F.; Zhou, L.; Liu, W. R.; Zhou, Z. C.; Yue, Q. H.; Zheng, W. Y.; Sun, R.; Liu, W. Y.; Xu, S. J.; Fan, H. J. et al. Organic solar cells with 18% efficiency enabled by an alloy acceptor: A two-in-one strategy. *Adv. Mater.* **2021**, *33*, 2100830.

[18] Ma, X. L.; Gao, W.; Yu, J. S.; An, Q. S.; Zhang, M.; Hu, Z. H.; Wang, J. X.; Tang, W. H.; Yang, C. L.; Zhang, F. J. Ternary nonfullerene polymer solar cells with efficiency > 13.7% by integrating the advantages of the materials and two binary cells. *Energy Environ. Sci.* **2018**, *11*, 2134–2141.

[19] Zhang, H.; Yao, H. F.; Hou, J. X.; Zhu, J.; Zhang, J. Q.; Li, W. N.; Yu, R. N.; Gao, B. W.; Zhang, S. Q.; Hou, J. H. Over 14% efficiency in organic solar cells enabled by chlorinated nonfullerene small-molecule acceptors. *Adv. Mater.* **2018**, *30*, 1800613.

[20] Zhou, D.; You, W.; Xu, H. T.; Tong, Y. F.; Hu, B.; Xie, Y.; Chen, L.

Recent progress in ternary organic solar cells based on solution-processed non-fullerene acceptors. *J. Mater. Chem. A* **2020**, *8*, 23096–23122.

[21] Yang, W. T.; Ye, L.; Yao, F. F.; Jin, C. H.; Ade, H.; Chen, H. Z. Black phosphorus nanoflakes as morphology modifier for efficient fullerene-free organic solar cells with high fill-factor and better morphological stability. *Nano Res.* **2019**, *12*, 777–783.

[22] Zhang, S. H.; Shah, M. N.; Liu, F.; Zhang, Z. Q.; Hu, Q.; Russell, T. P.; Shi, M. M.; Li, C. Z.; Chen, H. Z. Efficient and 1, 8-diiodooctane-free ternary organic solar cells fabricated via nanoscale morphology tuning using small-molecule dye additive. *Nano Res.* **2017**, *10*, 3765–3774.

[23] Hou, J. H.; Inganäs, O.; Friend, R. H.; Gao, F. Organic solar cells based on non-fullerene acceptors. *Nat. Mater.* **2018**, *17*, 119–128.

[24] Qian, D. P.; Zheng, Z. L.; Yao, H. F.; Tress, W.; Hopper, T. R.; Chen, S. L.; Li, S. S.; Liu, J.; Chen, S. S.; Zhang, J. B. et al. Design rules for minimizing voltage losses in high-efficiency organic solar cells. *Nat. Mater.* **2018**, *17*, 703–709.

[25] Liu, J.; Chen, S. S.; Qian, D. P.; Gautam, B.; Yang, G. F.; Zhao, J. B.; Bergqvist, J.; Zhang, F. L.; Ma, W.; Ade, H. et al. Fast charge separation in a non-fullerene organic solar cell with a small driving force. *Nat. Energy* **2016**, *1*, 16089.

[26] Vandewal, K.; Albrecht, S.; Hoke, E. T.; Graham, K. R.; Widmer, J.; Douglas, J. D.; Schubert, M.; Mateker, W. R.; Bloking, J. T.; Burkhard, G. F. et al. Efficient charge generation by relaxed charge-transfer states at organic interfaces. *Nat. Mater.* **2014**, *13*, 63–68.

[27] Vandewal, K.; Tvingstedt, K.; Gadisa, A.; Inganäs, O.; Manca, J. V. On the origin of the open-circuit voltage of polymer-fullerene solar cells. *Nat. Mater.* **2009**, *8*, 904–909.

[28] Benduhn, J.; Tvingstedt, K.; Piersimoni, F.; Ullbrich, S.; Fan, Y. L.; Tropiano, M.; McGarry, K. A.; Zeika, O.; Riede, M. K.; Douglas, C. J. et al. Intrinsic non-radiative voltage losses in fullerene-based organic solar cells. *Nat. Energy* **2017**, *2*, 17053.

[29] Vandewal, K.; Tvingstedt, K.; Gadisa, A.; Inganäs, O.; Manca, J. V. Relating the open-circuit voltage to interface molecular properties of donor: Acceptor bulk heterojunction solar cells. *Phys. Rev. B* **2010**, *81*, 125204.

[30] Liu, S. H.; Jiang, R. B.; You, P.; Zhu, X. Z.; Wang, J. F.; Yan, F. Au/Ag core-shell nanocuboids for high-efficiency organic solar cells with broadband plasmonic enhancement. *Energy Environ. Sci.* **2016**, *9*, 898–905.

[31] Qin, Y. P.; Zhang, S. Q.; Xu, Y.; Ye, L.; Wu, Y.; Kong, J. Y.; Xu, B. W.; Yao, H. F.; Ade, H.; Hou, J. H. Reduced nonradiative energy loss caused by aggregation of nonfullerene acceptor in organic solar cells. *Adv. Energy Mater.* **2019**, *9*, 1901823.

[32] Xie, Y. P.; Li, T. F.; Guo, J.; Bi, P. Q.; Xue, X. N.; Ryu, H. S.; Cai, Y. H.; Min, J.; Huo, L. J.; Hao, X. T. et al. Ternary organic solar cells with small nonradiative recombination loss. *ACS Energy Lett.* **2019**, *4*, 1196–1203.

[33] Xu, X. P.; Feng, K.; Lee, Y. W.; Woo, H. Y.; Zhang, G. J.; Peng, Q. Subtle polymer donor and molecular acceptor design enable efficient polymer solar cells with a very small energy loss. *Adv. Funct. Mater.* **2020**, *30*, 1907570.

[34] Ma, R. J.; Liu, T.; Luo, Z. H.; Gao, K.; Chen, K.; Zhang, G. Y.; Gao, W.; Xiao, Y. Q.; Lau, T. K.; Fan, Q. P. et al. Adding a third component with reduced miscibility and higher LUMO level enables efficient ternary organic solar cells. *ACS Energy Lett.* **2020**, *5*, 2711–2720.

[35] Chen, S. H.; Yan, T. T.; Fanady, B.; Song, W.; Ge, J. F.; Wei, Q.; Peng, R. X.; Chen, G. H.; Zou, Y. P.; Ge, Z. Y. High efficiency ternary organic solar cells enabled by compatible dual-donor strategy with planar conjugated structures. *Sci. China Chem.* **2020**, *63*, 917–923.

[36] Ma, Y. L.; Zhou, X. B.; Cai, D. D.; Tu, Q. S.; Ma, W.; Zheng, Q. D. A minimal benzo[*c*][1, 2, 5]thiadiazole-based electron acceptor as a third component material for ternary polymer solar cells with efficiencies exceeding 16.0%. *Mater. Horiz.* **2020**, *7*, 117–124.

[37] Wang, H. T.; Yang, L. Q.; Lin, P. C.; Chueh, C. C.; Liu, X.; Qu, S. Y.; Guang, S.; Yu, J. S.; Tang, W. H. A simple dithieno[3, 2-b: 2′, 3′-d]pyrrol-rhodanine molecular third component enables over 16. 7% efficiency and stable organic solar cells. *Small* **2021**, *17*, 2007746.

[38] Xu, L. Y.; Tao, W. X.; Liu, H.; Ning, J. H.; Huang, M. H.; Zhao, B.; Lu, X. H.; Tan, S. T. Achieving 17.38% efficiency of ternary organic solar cells enabled by a large-bandgap donor with noncovalent conformational locking. *J. Mater. Chem. A* **2021**, *9*, 11734–11740.

[39] Lee, S. M.; Kumari, T.; Lee, B.; Cho, Y.; Lee, J.; Oh, J.; Jeong, M.; Jung, S.; Yang, C. Horizontal-, vertical-, and cross-conjugated small molecules: Conjugated pathway-performance correlations along operation mechanisms in ternary non-fullerene organic solar cells. *Small* **2020**, *16*, 1905309.

[40] Ma, X. L.; Wang, J.; Gao, J. H.; Hu, Z. H.; Xu, C. Y.; Zhang, X. L.; Zhang, F. J. Achieving 17.4% efficiency of ternary organic photovoltaics with two well-compatible nonfullerene acceptors for minimizing energy loss. *Adv. Energy Mater.* **2020**, *10*, 2001404.

[41] Cui, Y.; Yao, H. F.; Zhang, J. Q.; Zhang, T.; Wang, Y. M.; Hong, L.; Xian, K. H.; Xu, B. W.; Zhang, S. Q.; Peng, J. et al. Over 16% efficiency organic photovoltaic cells enabled by a chlorinated acceptor with increased open-circuit voltages. *Nat. Commun.* **2019**, *10*, 2515.

[42] Liu, S.; Yuan, J.; Deng, W. Y.; Luo, M.; Xie, Y.; Liang, Q. B.; Zou, Y. P.; He, Z. C.; Wu, H. B.; Cao, Y. High-efficiency organic solar cells with low non-radiative recombination loss and low energetic disorder. *Nat. Photonics* **2020**, *14*, 300–305.

[43] Ma, Q.; Jia, Z. R.; Meng, L.; Zhang, J. Y.; Zhang, H. T.; Huang, W. C.; Yuan, J.; Gao, F.; Wan, Y.; Zhang, Z. J. et al. Promoting charge separation resulting in ternary organic solar cells efficiency over 17.5%. *Nano Energy* **2020**, *78*, 105272.

[44] Blom, P. W. M.; Mihailetchi, V. D.; Koster, L. J. A.; Markov, D. E. Device physics of polymer: Fullerene bulk heterojunction solar cells. *Adv. Mater.* **2007**, *19*, 1551–1566.

[45] Honda, S.; Ohkita, H.; Benten, H.; Ito, S. Selective dye loading at the heterojunction in polymer/fullerene solar cells. *Adv. Energy Mater.* **2011**, *1*, 588–598.

[46] Cheng, T. W.; Keskkula, H.; Paul, D. R. Property and morphology relationships for ternary blends of polycarbonate, brittle polymers and an impact modifier. *Polymer* **1992**, *33*, 1606–1619.

[47] Li, D.; Neumann, A. W. A reformulation of the equation of state for interfacial tensions. *J. Colloid Interface Sci.* **1990**, *137*, 304–307.

[48] Nilsson, S.; Bernasik, A.; Budkowski, A.; Moons, E. Morphology and phase segregation of spin-casted films of polyfluorene/PCBM blends. *Macromolecules* **2007**, *40*, 8291–8301.

[49] Clint, J. H. Adhesion and components of solid surface energies. *Curr. Opin. Colloid Interface Sci.* **2001**, *6*, 28–33.

[50] Makkonen, L. Young's equation revisited. *J. Phys. :Condens. Matter* **2016**, *28*, 135001.

[51] Adil, M. A.; Zhang, J. Q.; Wang, Y. H.; Yu, J. D.; Yang, C.; Lu, G. H.; Wei, Z. X. Regulating the phase separation of ternary organic solar cells via 3D architectured AIE molecules. *Nano Energy* **2020**, *68*, 104271.

[52] Ye, L.; Hu, H. W.; Ghasemi, M.; Wang, T. H.; Collins, B. A.; Kim, J. H.; Jiang, K.; Carpenter, J. H.; Li, H.; Li, Z. K. et al. Quantitative relations between interaction parameter, miscibility and function in organic solar cells. *Nat. Mater.* **2018**, *17*, 253–260.

[53] Fan, H. Y.; Yang, H.; Wu, Y.; Yildiz, O.; Zhu, X. M.; Marszalek, T.; Blom, P. W. M.; Cui, C. H.; Li, Y. F. Anthracene-assisted morphology optimization in photoactive layer for high-efficiency polymer solar cells. *Adv. Funct. Mater.* **2021**, *31*, 2103944.

[54] Zhang, X. Q.; Liu, M. Y.; Yang, B.; Zhang, X. Y.; Chi, Z. G.; Liu, S. W.; Xu, J. R.; Wei, Y. Cross-linkable aggregation induced emission dye based red fluorescent organic nanoparticles and their cell imaging applications. *Polym. Chem.* **2013**, *4*, 5060–5064.